State-dependent FRET reports calcium- and voltage-dependent gating-ring motions in BK channels

Pablo Miranda[a,b,1], Jorge E. Contreras[c,1,2], Andrew J. R. Plested[d,e], Fred J. Sigworth[f], Miguel Holmgren[c], and Teresa Giraldez[a,3]

[a]Research Division, University Hospital of Nuestra Señora de Candelaria, 38010 Tenerife, Spain; [b]Department of Physiology, University of La Laguna, 38071 Tenerife, Spain; [c]National Institute of Neurological Disorders and Stroke, National Institutes of Health, Bethesda, MD 20892; [d]Leibniz-Institut für Molekulare Pharmakologie, 13125 Berlin, Germany; [e]NeuroCure, Charité-Universitätsmedizin Berlin, 10117 Berlin, Germany; and [f]Department of Cellular and Molecular Physiology, Yale University School of Medicine, New Haven, CT 06520

Edited by Ramon Latorre, Centro Interdisciplinario de Neurociencias, Universidad de Valparaíso, Valparaíso, Chile, and approved February 11, 2013 (received for review November 13, 2012)

Large-conductance voltage- and calcium-dependent potassium channels (BK, "Big K+") are important controllers of cell excitability. In the BK channel, a large C-terminal intracellular region containing a "gating-ring" structure has been proposed to transduce Ca^{2+} binding into channel opening. Using patch-clamp fluorometry, we have investigated the calcium and voltage dependence of conformational changes of the gating-ring region of BK channels, while simultaneously monitoring channel conductance. Fluorescence resonance energy transfer (FRET) between fluorescent protein inserts indicates that Ca^{2+} binding produces structural changes of the gating ring that are much larger than those predicted by current X-ray crystal structures of isolated gating rings.

allosteric regulation | SLO1 channel | fluorescence

Large-conductance voltage- and calcium-dependent (BK) potassium channels are characterized by both their large single-channel conductance and their synergistic activation by Ca^{2+} and membrane depolarization (1). These channels are crucial regulators of physiological processes such as neurosecretion, neuronal firing, and smooth muscle tone (2). In humans, defects in BK channels can cause hypertension, cancer, and epilepsy (3–5).

BK channels at the plasma membrane are homotetramers of α-subunits, which can assemble with various accessory subunits. The α-subunits, encoded by the potassium large-conductance calcium-activated channel, subfamily M, α member 1 (KCNMA1) gene, consist of seven membrane-spanning regions (S0–S6) and a large intracellular C-terminal domain (Fig. 1*A*) (1). In common with other voltage-gated channels, the voltage sensor resides within the membrane (6), whereas Ca^{2+} binds to binding sites located at a large C-terminal intracellular region where eight regulator of conductance for K^+ (RCK) domains form a "gating ring" (7–11).

Kinetic modeling of the Ca^{2+}- and voltage-dependent activation of BK channels suggests that fairly complex mechanisms are required to describe channel activity (12–16). Biochemical studies of isolated gating rings in vitro indicate that RCK domains undergo structural rearrangements upon Ca^{2+} binding (17). Several lines of evidence support a model in which Ca^{2+} binding expands the gating ring and physically pulls open the pore helices, opening the channel gate (11, 18, 19).

Recently, structures of gating rings isolated from eukaryotic channels have been solved (9, 10), and in the most recent X-ray structure obtained in the presence of Ca^{2+} (11) the layer formed by the four RCK1 domains of the tetramer is seen to be expanded relative to the previous structures by more than 10 Å. Because this region of the gating ring is directly linked to the channel's pore-forming helices, this expansion could be the direct link between Ca^{2+} binding and the opening of the pore in BK channels.

To measure directly the conformational changes between subunits at the level of the gating ring, during the activation of functional BK channels, we performed patch-clamp fluorometry (20) on membrane patches containing fluorescently labeled BK channels. These channels were selected from a library of functional YFP- or CFP-fusion proteins (21). Simultaneous optical and electrical recording revealed large changes in fluorescence resonance energy transfer (FRET) accompanying Ca^{2+} binding and channel activation.

Results

Heterotetramers containing α-subunits tagged with CFP or YFP at identical insertion positions were coexpressed in *Xenopus* oocytes (Fig. 1*B* and Fig. S1). FRET signals and K^+ currents were recorded simultaneously from excised macropatches, while the membrane potential, and the Ca^{2+} concentration at the intracellular side, were varied (Fig. S2). The relative movement of equivalent sites in the gating-ring tetramer was estimated from changes in FRET between CFP and YFP tags, quantified as the energy transfer efficiency E calculated from emission spectral ratios (*Methods* and Fig. S3). We studied the relative movement of subunits at three different locations within the BK channel's gating ring (Fig. 1): the site at residue 667 (located in the linker between RCK1 and RCK2), the 860 site (RCK2 domain), and the 901 site, adjacent to the Ca^{2+} binding site known as the "calcium bowl."

Fig. 1 *C* and *D* illustrates approximate locations of the three sites in "resting" and "open" gating-ring structures. Two nearly identical crystal structures of gating rings from eukaryotes have been proposed to reflect the structure of the gating ring in the resting state [Protein Data Bank (PDB) ID codes 3NAF (10) and 3MT5 (9)]; meanwhile a third structure, obtained in the presence of calcium, is proposed to reflect an "open" conformation that could activate the channel [3U6N (11)]. The 860 site is missing from these structures, so the closest resolved residues (D833 and T872) are shown as blue in Fig. 1 *C* and *D*. The 667 site is contained within a short disordered region in the long linker between RCK1 and RCK2 domains. In the Ca^{2+}-free structure, the residue 666 is resolved, allowing the approximate position of the 667 insertion to be identified directly in that structure (Fig. 1 *C* and *D*, *Left*, magenta residues). In the "open" structure, a longer region is unstructured, flanked by residues F609 and K684 (Fig. 1 *C* and *D*, green residues). Comparison of *Left* and *Right* within Fig. 1 *C* and *D* shows that, in the isolated gating ring, the insertions at 667 and 860 positions are expected to show

Author contributions: P.M., F.J.S., M.H., and T.G. designed research; P.M., J.E.C., and T.G. performed research; P.M., A.J.R.P., F.J.S., M.H., and T.G. analyzed data; and P.M., J.E.C., A. J.R.P., F.J.S., M.H., and T.G. wrote the paper.

The authors declare no conflict of interest.

This article is a PNAS Direct Submission.

[1]P.M. and J.E.C. contributed equally to this work.

[2]Present address: Department of Pharmacology and Physiology, University of Medicine and Dentistry of New Jersey, Newark, NJ 07103.

[3]To whom correspondence should be addressed. E-mail: giraldez@ull.es.

This article contains supporting information online at www.pnas.org/lookup/suppl/doi:10.1073/pnas.1219611110/-/DCSupplemental.

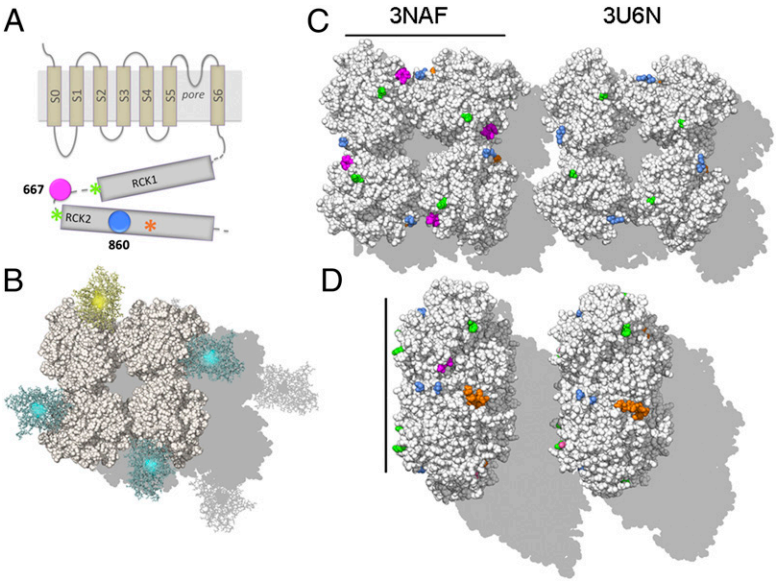

Fig. 1. Localization of the fluorescent reporters in the BK gating-ring structure. (*A*) Topological representation of the BK α-subunit. The transmembrane region includes the voltage sensing domain (S1–S4), the pore domain (S5–S6) and an additional transmembrane helix (S0) that leads the N terminus to the extracellular side. The large cytoplasmic region consists of two RCK domains (RCK1 and RCK2). The orange asterisk indicates high-affinity Ca^{2+} binding site at RCK2 (calcium bowl). Amino acid positions where the fluorescent protein sequence was inserted are shown in blue (BK-860) or in magenta (BK-667). The green asterisks indicate amino acids flanking the disordered loop containing the 667 site. The native human BK numbering (23) is given for the constructs used in this study. (*B*) Structures of fluorescent proteins CFP and YFP (cyan and yellow, respectively) are represented as linked at position 667 in each subunit of the Ca^{2+}-free gating ring structure (3NAF) (10). In this model, the neighboring fluorophores are 95 Å apart. Quantified RNA was injected in a 3:1 ratio into *Xenopus* oocytes to express most frequently the fluorescent heterotetramer 3CFP:1YCFP BK (Fig. S1) that is illustrated. (*C*) Ca^{2+}-free (PDB ID code 3NAF; *Left*) and Ca^{2+}-bound "open" (PDB ID code 3U6N; *Right*) structures of the gating ring, viewed toward the membrane plane. Colors follow the same code as the scheme shown in *A*. The 667 sites were resolved only in the Ca^{2+}-free structure (*Left*; highlighted in magenta). For comparison, boundaries of regions comprising the 667 sites (F609 and K684) are labeled in both structures (green). The 860 site resides in an unresolved loop region between positions D833 and T872 (blue). (*D*) Side view of the gating ring with the same sites highlighted. The transmembrane region would lie to the right in this view. (Scale bars in *C* and *D*: 100 Å.)

only small displacements upon Ca^{2+} binding to the high-affinity Ca^{2+} binding site situated at the RCK2 domain (calcium bowl; Fig. 1 *C* and *D*, orange residues).

Fig. 2 *A* and *D* shows the robust potassium currents recorded in membrane patches from *Xenopus* oocytes expressing the heteromers of BK-667CFP and BK-667YFP, or BK-860CFP and BK-860YFP channel constructs, respectively. These heteromers are denoted BK-667CY and BK-860CY. As we previously showed (21), insertions of fluorescent proteins at these sites have little influence on the voltage and calcium sensitivity. When the cyan fluorescent subunits of these channels were excited with 458-nm light, the acquired emission spectra showed a variable FRET signal near 530 nm corresponding to YFP fluorescence (Fig. 2 *B* and *E*, *Upper*; *Methods*; and Fig. S3), whereas the pure YFP emission remained unaltered (Fig. 2 *B* and *E*, *Lower*). The estimates of FRET efficiency *E* revealed, in the case of BK-667CY channels, substantial changes with voltage (Fig. 2*C*) and calcium (see below), and in the case of BK-860CY (Fig. 2*F*), a large change with Ca^{2+} concentration alone.

Ca^{2+} Induces Separation of the 860 Sites Within the RCK2 Domains. We used the conductance voltage (*G–V*) relationship as an index of the increase in channel open probability with voltage. These *G–V* curves are Ca^{2+} dependent, as shown in Fig. 3*A* for the expressed heteromers BK-860CY. As Ca^{2+} was increased from 0 to 95 μM, the half-activation potential $V_{1/2}$ shifted from +137.5 to –17.3 mV (Fig. 3*A*, *Upper*). The *G–V* curves could be well described by an allosteric model (16) (Fig. 3*A*, *Upper*, solid lines) with parameters as given in Table S1. Fluorescence data were acquired simultaneously with the *G–V* curves and are plotted in Fig. 3*A* (*Lower*). In nominally Ca^{2+}-free solutions and at low Ca^{2+} concentration of 0.7 μM, the energy transfer efficiency from CFP to YFP showed a high value $E = 0.54 \pm 0.05$ ($n = 8$; Fig. 3*A*, *Lower*), consistent with a distance *r* between neighboring fluorophores of about 60 Å. This distance estimate takes into account the presence of different combinations of CFP donors and YFP acceptors, using the value $R_0 = 50$ Å for the CFP–YFP pair (*Methods*; see Fig. S7; and ref. 22).

As $[Ca^{2+}]$ increased, the mean *E* value gradually decreased to reach a value of $E = 0.039 \pm 0.003$ ($n = 9$) at 95 μM free Ca^{2+} (Fig. 3*A*, *Lower*). This value is consistent with the separation between chromophores being at least 90 Å (roughly $2R_0$). It is remarkable that there is no variation of *E* with membrane potential up to 200 mV, at any of the studied Ca^{2+} concentrations. However, Ca^{2+} still caused a strong hyperpolarizing shift of the *G–V* curve (Fig. 3*A*, *Upper*), indistinguishable from the effect observed in wild-type channels (23, 24).

To confirm that the observed movement of the 860 site in RCK2 is due to Ca^{2+} binding, we sequentially mutated two high-affinity Ca^{2+} binding sites that reside in the gating ring. First, we mutated the site known as the calcium bowl, which resides in a highly conserved region rich in aspartate residues (DQDDDDDPD) of the RCK2 domain (25–27). The other site, situated in the RCK1 domain, can be neutralized by mutations at D362 and D367, or E535 (28, 29). Mutation of the M513 site has been reported to affect Ca^{2+} binding at the RCK1 site as well (23, 29).

We first generated the construct BK-860/5D5A by mutating the calcium bowl's five aspartates D894-898 to alanines. The ability of Ca^{2+} to activate and shift gating of BK-860/5D5A/CY channels is markedly reduced relative to BK-860CY channels (Fig. 3*B*, *Upper*; compare with Fig. 3*A*, *Upper*) even though these mutations do not disrupt the channel Ca^{2+} sensitivity completely, as seen previously (5, 23, 25, 26, 28, 30). Throughout the voltage range, *E* values remained at 0.61 ± 0.02 ($n = 6$) for low Ca^{2+} concentrations; this FRET value is indistinguishable from those obtained at low Ca^{2+} with BK-860CY channels (Fig. 3*A*, *Lower*, black and purple traces), suggesting that the BK-860CY and BK-860/5D5A/CY channels have a similar conformation at low intracellular Ca^{2+}. However, when intracellular Ca^{2+} was increased to 95 μM for BK-860/5D5A/CY, we detected a decrease in *E* values to 0.454 ± 0.004 ($n = 3$; Fig. 3*B*, *Lower*), a much smaller decrease than observed when the calcium bowl was intact (Fig. 3*A*, *Lower*). By further disrupting the channels' Ca^{2+} sensitivity with the additional M513I mutation (23, 29) (Fig. 3*C*, *Upper*), we essentially abolished all Ca^{2+}-dependent changes of the FRET signals (Fig. 3*C*, *Lower*). These results are additionally supported by experiments with construct BK-901CY, where GFP analogs were inserted at the residue 901 site, in the calcium bowl (21). In this case, we obtained channels with altered Ca^{2+} sensitivity, but we observed only small differences in FRET values at low and high Ca^{2+}

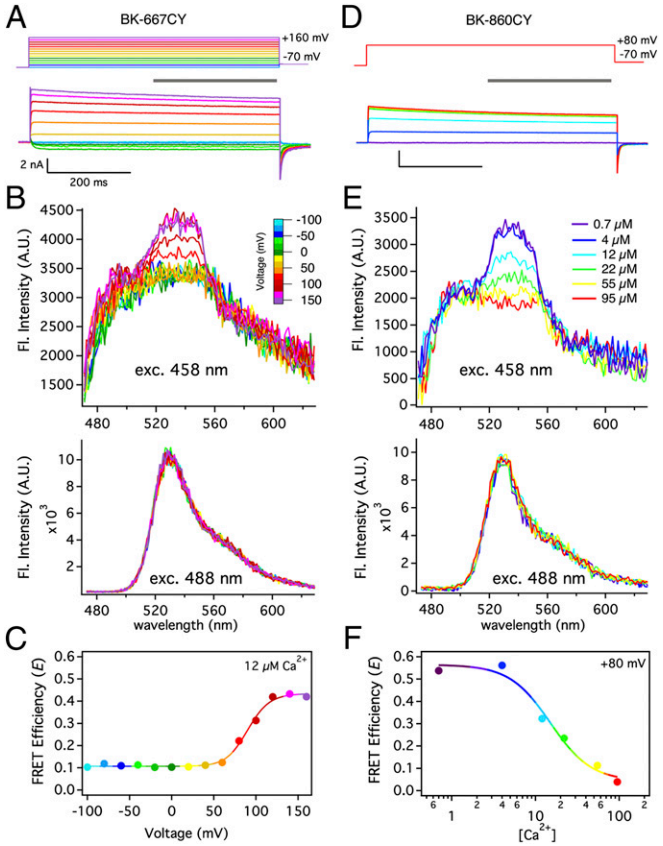

Fig. 2. Ca^{2+} and voltage induce structural rearrangements of the gating ring of intact BK channels in membrane macropatches. (*A*) Depolarizing pulses (upper traces) were applied to a *Xenopus* oocyte inside-out patch in 12 μM Ca^{2+}, evoking the current traces shown beneath. Depolarizations were followed by a −70 mV repolarizing pulse and the holding potential was −100 mV. (*B*) Fluorescence spectra collected from the patch in *A* during steady-state activation (gray bar in *A*; Fig. S2). Excitation with 458-nm light produced mixed CFP and YFP emission (*Upper*), whereas 488-nm light drove only YFP emission (*Lower*). Traces are drawn with the same color coding according to voltage (color scale bar). (*C*) FRET efficiency *E* calculated from spectra at all studied voltages. The solid line is a Boltzmann fit. (*D*) Representative BK-860CY currents recorded from a *Xenopus* oocyte inside-out patch in various Ca^{2+} concentrations but with a fixed depolarization to +80 mV. Current traces are color-coded according to the free Ca^{2+} concentration (legend in *E*). (*E*) Synchronous fluorescence recordings for the same patch as *D*. (*F*) The dependence of FRET efficiency (*E*) on [Ca^{2+}] (circles) was fitted to a Hill function (solid line) with k_d = 16 μM and n = 1.8.

concentrations (Fig. S4). Altogether, these results show that the Ca^{2+}-induced dynamics of the gating ring are related to the channel's ability to respond to intracellular Ca^{2+} concentration.

Sites at the RCK1–RCK2 Linkers Move Closer in a Ca^{2+}- and Voltage-Dependent Manner. We next measured FRET at the 667 site situated within the RCK1–RCK2 linker domain. We applied membrane potentials from −100 to +200 mV, a range that was sufficiently broad that, at every Ca^{2+} concentration studied, the channels move from fully closed to fully open states (Fig. 4*A*, *Upper*). At nominally zero Ca^{2+} and 0.7 μM Ca^{2+}, we obtained a low FRET efficiency $E = 0.063 \pm 0.003$ (n = 13; Fig. 4*A*, *Lower*), independent of the membrane potential and consistent with the fluorophores at 667 sites of adjacent subunits remaining at a distance of about 90 Å apart. However, when Ca^{2+} concentration was in the range of 4–55 μM, the energy transfer increased in a voltage-dependent manner, indicating that depolarization increases the probability that the 667 sites are close together. At higher calcium, *E* again becomes voltage independent, saturating at 0.50 ± 0.01 (n = 4), consistent with fluorophores inserted at neighboring 667 sites moving together to a spacing of nearly 60 Å.

Sequential mutations to disrupt the high-affinity Ca^{2+} binding sites of the BK-667 constructs were performed to explore the relationship of the observed FRET changes to Ca^{2+} binding. As we observed for the BK-860 constructs, mutation of the calcium bowl (BK-667/5D5A/CY) reduced the channel's Ca^{2+} sensitivity, which was reflected in a right shift of the *G–V* curves compared with BK-667CY channels, at all Ca^{2+} concentrations (Fig. 4*B*, *Upper*). At low Ca^{2+} concentrations (0.7–12 μM), the BK-667/5D5A/CY mutant had an average voltage-independent *E* value of 0.15 ± 0.03 (n = 18), and at high Ca^{2+} concentrations (70–95 μM) *E* saturated at 0.35 ± 0.01. Interestingly, at intermediate Ca^{2+} concentrations (12 and 22 μM), despite the smaller range of *E* values, the FRET signal clearly showed a voltage dependence (Fig. 4*B*, *Lower*, cyan and green symbols). Similarly to our observations with the BK-860 construct mutations, additional disruption of the M513 site all but abolished Ca^{2+}- and voltage-dependent changes in *E* (Fig. 4*C*, *Lower*).

FRET efficiency is very sensitive to changes in the separation between fluorophores, but it can also be affected by their relative orientations (31). Both the 667 and 860 insertion sites are in flexible loops, which could allow a range of fluorophore orientations. We performed anisotropy measurements for BK-860CY and BK-667CY channels in excised membrane patches at +80 mV and Ca^{2+} concentrations of 0.7 and 95 μM to test for the mobility of the attached fluorescent proteins (32). In all conditions tested, we obtained a similar anisotropy value of ∼0.2 (*Methods*), significantly lower than that of an immobile fluorophore [tetramethylrhodamine methyl ester (TMRM) in glycerol, anisotropy of 0.38; *Methods*]. This result is consistent with other studies showing reasonable flexibility of GFP molecules fused to other proteins, including ion channels, under physiological conditions (33, 34). The low anisotropies support the assumption that the variations in *E* are mainly due to changes in distance between the fluorescent probes.

Discussion

With fluorescent-protein labels inserted in each BK subunit at either residue 860 or residue 667, there are large Ca^{2+}-dependent changes in resonance energy transfer (FRET). These changes reflect large movements of the BK gating ring, in which an apparent fluorophore spacing of at least 90 Å between neighboring positions on equivalent subunits (for example, as illustrated in Fig. 1*B*) changes to a spacing of about 60 Å. This motion is much larger than that proposed by Yuan et al. (11) in a comparison of two crystal structures of isolated gating rings. A further surprise is that the FRET changes do not track the channel's open probability, but are less sensitive to voltage than the *G–V* relationship; indeed, the changes at position 860 have no discernable voltage dependence and have distinct Ca^{2+} dependence from the changes at position 667.

How is it possible that Ca^{2+}-dependent FRET signals from one part of the gating ring have voltage dependence and those from another do not, whereas both reporter sites show calcium dependence? A simple explanation would be that there are multiple calcium-driven conformational changes in the gating ring, some of which are sensitive to voltage (like those detected by fluorophores inserted at 667 at intermediate Ca^{2+} concentrations) and some that are largely voltage independent (such as the site 860).

The very successful allosteric model of BK channel activation of Horrigan and Aldrich (15) and its extensions (16, 35, 36) (Fig. S5*A*)—we will call them collectively the standard model—postulate that the Ca^{2+} binding sites are allosterically coupled to the channel open–closed transition. That is, each of the one or more channel-activating Ca^{2+} binding sites on each subunit has a higher affinity when the channel is open than when it is closed,

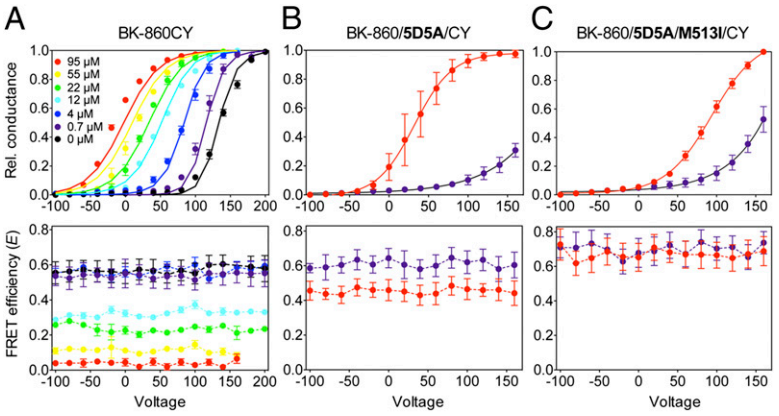

Fig. 3. Relative movement of the 860 sites shows Ca^{2+} dependence. *G–V* curves (upper panels) and FRET efficiency (*E–V*) curves (lower panels) were determined synchronously from patches at various free Ca^{2+} concentrations, for BK-860CY heterotetramers (*A*), and (*B*) mutants with disrupted Ca^{2+} sensitivity at the Ca^{2+} bowl (BK-860/5D5A/CY), or (*C*) at both the calcium bowl and the RCK1 Ca^{2+} binding site (BK-860/5D5A/M513I/CY). Data are color-coded in all graphs according to free Ca^{2+} concentration. The solid curves in *A* (*Upper*) represent fits to the Sweet and Cox (16) model with parameters shown in Table S1. Data points and error bars represent average ± SEM (n = 3–13).

and this change in affinity helps drive the opening of the channel in the presence of intracellular Ca^{2+}. Since channel opening is strongly voltage dependent, Ca^{2+} binding to these sites will necessarily show a strong voltage dependence.

The entirely voltage-independent FRET signal from the 860 site therefore cannot arise from any of the transitions within the standard model, because all of those transitions are strongly coupled to one another. Instead, the signal must reflect a conformational change that is uncoupled from channel opening. The simplest explanation for this signal is that it comes from a conformational change in an uncharted Ca^{2+} binding site that does not participate in channel activation. Alternatively, it could come from a motion of the gating ring that is uncoupled from the motions coupled to channel opening. That mutations in two putative activating Ca^{2+} binding sites suppress this conformational change may reflect a general reduction in mobility of the gating ring caused by the mutations. The FRET vs. $[Ca^{2+}]$ relationship (Fig. 2*F*) shows a Hill slope of 2, consistent with the idea that Ca^{2+} binding in two or more sites (either within individual subunits, or in multiple subunits) must occur to produce the FRET signal from insertions at 860.

More complex is the case of the signal from the 667 site. That signal has the remarkable property that it saturates at low and high Ca^{2+} concentrations, but in an intermediate range it shows voltage dependence in addition to its Ca^{2+} dependence. We reasoned that a calcium binding site that changes its affinity in response to the state of the BK voltage sensors or to channel opening would be expected to show the proper combination of saturation and voltage dependence depending on Ca^{2+} concentration and therefore could give rise to the FRET signal as reflected in the *E–V* relationship. The Ca^{2+} dependence of *G–V* can be well described with the Sweet and Cox (16) allosteric model (Figs. 3*A* and 4*A*, *Upper*, solid curves), which postulates two Ca^{2+} binding sites in each subunit. Nevertheless, this model cannot well describe the *G–V* and *E–V* relationships simultaneously (Fig. S5*A*). The reason has to do with the strong coupling in the standard model between Ca^{2+} binding events, the channel-opening transition, and activation of the voltage sensors. The strong coupling means that it is impossible to have a substantially different voltage dependence for one equilibrium in the model than for another. Consider the *E–V* relationship at 4 μM (Fig. 4*A*, *Lower*, blue curve). Its midpoint voltage is +120 mV, whereas the corresponding midpoint voltage of channel opening is +70 mV. We could not find a way to adapt the standard model to describe these differing voltage dependences. We explored a large number of modifications of the standard model with various sources for the FRET signal (it might arise directly from Ca^{2+} binding events, or from conformational changes) and tried interposing new transitions into the pathway between Ca^{2+} binding and channel activation, or between Ca^{2+} binding and voltage sensor activation. Most models failed to describe the data, or mandated assumptions inconsistent with previous experimental data. An example (Fig. S5*B*) would be the introduction of an additional voltage-dependent transition to the voltage sensor, similar to that observed in other potassium channels (37). This modification appears to be inconsistent with BK channel gating currents, because *Q–V* curves are not biphasic (15, 38). Further work will be required to unify the descriptions of the optical and electrical data in a single activation mechanism. So far, we conclude that, to explain simultaneously the movement of the gating ring and the channel gating, the standard model would have to be extended by including additional Ca^{2+} binding sites, or additional voltage dependences, or by relaxing the assumption of linearly additive energies of interaction in the allosteric scheme.

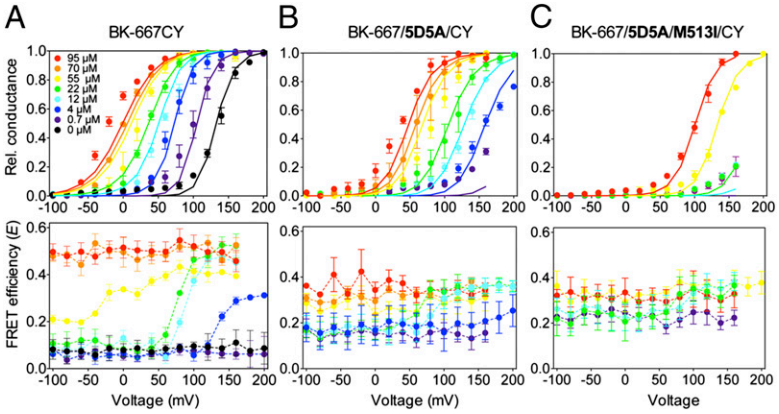

Fig. 4. Relative movement of the 667 sites is Ca^{2+} and voltage dependent. *G–V* curves (*Upper*) and the corresponding *E–V* curves (*Lower*) were determined synchronously at various free Ca^{2+} concentrations, for (*A*) BK-667CY heterotetramers, (*B*) mutants with reduced Ca^{2+} sensitivity at the Ca^{2+} bowl (BK-667/5D5A/CY), or (*C*) mutations at both the Ca^{2+} bowl and the RCK1 Ca^{2+} binding site (BK-667/5D5A/M513I/CY). Data are color-coded in all graphs according to free Ca^{2+} concentrations. The solid lines in *A–C* (*Upper*) represent fits to the Sweet and Cox (16) model with parameters shown in Table S1. Data points and error bars represent average ± SEM (n = 3–13).

What structural change could account for the very large FRET changes, which correspond to remarkable changes in spacing of the fluorophores between at least 90 Å and nearly 60 Å? When [Ca^{2+}] increases, the 667 site regions located at the four linkers between RCK1 and RCK2 domains move closer to each other, whereas the 860 site regions at the RCK2 domains move apart, suggesting a rotation. Elaboration of a precise structural model is not feasible because the loop containing residue 860 is not resolved in crystal structures of the BK gating ring (9–11). Therefore, the position of fluorescent proteins inserted at 860 cannot readily be related to our FRET results. In contrast, the fluorophores inserted at position 667 can be placed without much ambiguity, allowing us to map dynamic information about their movements during gating onto the existing static structural data. We sought to obtain a qualitative explanation for the FRET signal in BK667CY by searching a collection of 1,000 randomly generated rigid-body rotations of individual subunits within the gating ring. We looked for rotation axes and angles that could explain the distance changes while avoiding clashes (*Methods*). Large rotations gave on average more overlaps (Fig. S6), but 585 of the 1,000 random rotations yielded <1% of the atoms overlapping. However, only a few rotations yielded models with < 1% overlapping atoms, more than 5 Å net outward movement of the S6 linker and, simultaneously, the approach of neighboring 667 positions by more than 20 Å (Fig. S6). Examining intersubunit clashes at 1° intervals for a selection of these rotation axes revealed that most had implausible steric clashes along the rotation path, but an example model that had only minor clashes (Fig. S6) is shown in Fig. 5. This model, which is generated by a 30° rotation of each subunit, brings the fluorophores at 667 closer together by 40 Å, to their closest possible position, moves the S6 linker outward by 5 Å, and would tend to separate the insertions at 860 (Fig. S6), also displacing the calcium bowl from its intersubunit location. Of course, other motions are possible, of which intrasubunit conformational changes seem to us the most likely, but this analysis demonstrates the extent of the movements that are required to describe our data.

In summary, we have demonstrated in intact BK channels that there are remarkably large rearrangements of the gating ring upon Ca^{2+} binding, much larger than the rearrangements predicted by existing X-ray structures of the isolated gating ring. From the kinetic perspective, these rearrangements are puzzling because they do not have a simple relationship to the open–closed transition of the ion channel, and thus motivate the development of new models of BK channel activation. Using the existing structural data, the movement can be explained qualitatively by rotation of the individual subunits.

Methods

Molecular Biology and Heterologous Expression of BK Constructs. Human BKα (GenBank accession number U11058) fluorescent constructs BK-667, BK-860, and BK-901 were selected from a library of functional BK fluorescent proteins obtained previously (21) and expressed in *Xenopus laevis* oocytes. CFP- and YFP-fusion construct RNAs were combined (3:1 ratio) to enrich the channel population in 3CFP:1YFP labeled tetramers (Fig. S1). Mutagenesis, RNA transcription, and cell transfection were performed using standard procedures.

Patch-Clamp Fluorometry and FRET Efficiency Calculations. Inside-out patches were excised using pipettes with large tip apertures (~600-kΩ resistance values in symmetrical K^+) and currents were recorded with the Axopatch 200B amplifier and Clampex software (Molecular Devices). Recording solutions contained the following (in mM): pipette, 40 $KMeSO_3$, 100 *N*-methylglucamine-$MeSO_3$, 20 Hepes, 2 KCl, 2 $MgCl_2$, 95 μM $CaCl_2$ (pH 7.4); bath solution, 40 $KMeSO_3$, 100 *N*-methylglucamine-$MeSO_3$, 20 Hepes, 2 KCl, 1 HEDTA, and $CaCl_2$ to give the appropriate free Ca^{2+} concentration. No Ca^{2+} chelator was used in solutions containing 70 μM Ca^{2+} or higher. The amount of total $CaCl_2$ needed to obtain the desired free Ca^{2+} concentration was calculated using the program Max Chelator (39), which was downloaded from http://maxchelator.stanford.edu. Free Ca^{2+} concentrations were verified with a Ca^{2+}-sensitive electrode (Orion electrode; Thermo Lab Systems).

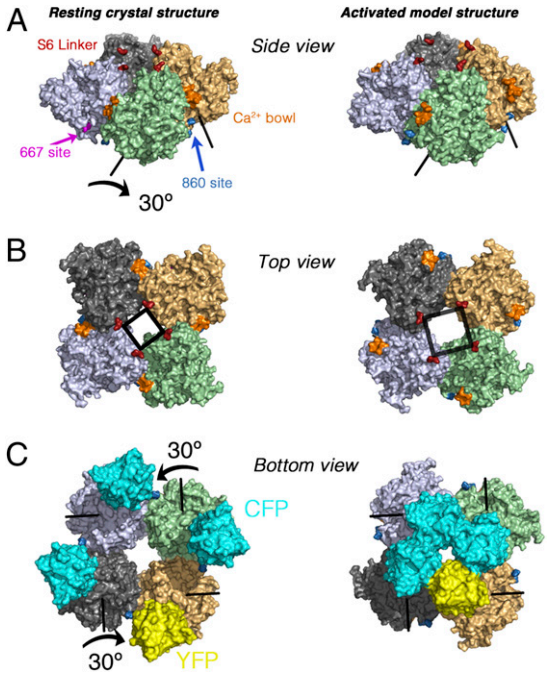

Fig. 5. Model of the gating ring movement. (*A*) Side view of the Ca^{2+}-free gating ring (3NAF structure) before (*Left*) and after (*Right*) applying a rotation of 30° (indicated with arrows) of each subunit around the individual rotation axes shown. The transmembrane region would lie above the gating ring in this view. The Ca^{2+} bowl is shown in orange, and the S6 linkers in red. (*B*) Corresponding top view. Note the predicted separation of the S6 segments (black square). (*C*) Bottom view of the fluorescent fusion BK-667CY gating ring model. In addition to separating the S6 linker segments, the 30° rotation of each RCK1–RCK2 module moves the fused fluorescent proteins at positions 667 closer together by 40 Å (*Right*).

The predicted free Ca^{2+} in nominal "zero calcium" solutions was approximately 60-80 nM, assuming 10-20 nM contaminant Ca^{2+}. Ca^{2+} solutions were exchanged using a fast solution-exchange perfusion system (BioLogic). To generate the conductance–voltage (*G–V*) curves, current amplitudes were extrapolated after fitting exponential functions to the decaying tail currents and normalized to the maximum extrapolated tail current. Excitation sources for CFP and YFP (458 and 488 nm, respectively) originated from an argon laser (Spectra-Physics). Emission light from the patch was delimited with a slit and scattered by the spectrograph's diffraction grating (Spectra-Physics) onto a CCD camera (Princeton Instruments). This allowed recording the emission spectrum of the patch in a single image of 250-ms exposure time, during every depolarizing pulse (Fig. S2). Analysis was performed using emission spectra ratios RatioA and $RatioA_0$ (Fig. S3) as described elsewhere (20). The apparent maximal FRET value ($RatioA_1$) was measured as the emission ratio of YFP for cells expressing a YFP–CFP tandem construct in which fluorescent proteins are linked by a 24-aa linker, kindly provided by J. Zheng (University of California, Davis, CA). FRET efficiency *E* was calculated as $E = (\text{RatioA} - \text{RatioA}_0)/(\text{RatioA}_1 - \text{RatioA}_0) = F_{458}^{FRET} \Big/ F_{458}^{FRET,max}$ (34). In our experiments, the majority of the FRET signal originates from heteromers formed by three CFP donors for each YFP acceptor, and additionally from two donors for two acceptors (Fig. S1). To a very good approximation (Fig. S7), *E* depends on the distance *r* between neighboring fluorophores according to the following:

$$E = \frac{1.4}{\left(\frac{0.98r}{R_0}\right)^6 + 1},$$

where the Förster distance R_0 for the CFP–YFP pair was taken to be 50 Å, and the absence of orientational constraints on the fluorophores was assumed.

Anisotropy Measurements. To test for orientational constraints, anisotropy was measured on inside-out membrane patches containing fluorescently labeled channels as described elsewhere (34, 40). An excitation polarizer was

PHYSIOLOGY

placed in front of the excitation filter, and two emission polarizers were positioned directly below the emission filter, one in a parallel (||) and the other in a perpendicular (⊥) orientation. We calculated the steady-state anisotropy A with the equation $A = (I_{||} - GI_{\perp})/(I_{||} + 2GI_{\perp})$. To determine the intrinsic polarization properties of the optical system, we measured the anisotropy of TMRM (Invitrogen) dissolved in glycerol (32). In our system, the value obtained for TMRM anisotropy was exactly 0.38 as previously described (32), so we used a G factor of 1 to calibrate channel anisotropy values. Measured values were as follows: BK-667: 0.19 ± 0.04; $n = 3$ at 0.7 μM Ca^{2+}; and 0.22 ± 0.01; $n = 3$ at 95 μM Ca^{2+}; BK-860: 0.20 ± 0.02; $n = 3$ at 0.7 μM Ca^{2+}; and 0.20 ± 0.01; $n = 2$ at 95 μM Ca^{2+}.

Data Modeling. *G–V* curves were fitted with open probabilities computed from the two-site allosteric model of Sweet and Cox (16) (Table S1). Additional modeling used in this study is described in Fig. S5.

Generation of a Structural Model for the FRET Signal. Each of the four individual subunits in the BK channel gating ring (from the Ca^{2+}-free "resting" structure 3NAF) was treated as a rigid body and rotated by a random extent (5–40°) around a randomly chosen axis. The equivalent rotation was applied to each of the subunits to maintain fourfold symmetry, and an ensemble of 1,000 random rotations was accumulated. We evaluated the interfluorophore distances and the position of the S6 linker, as well as the intermolecular clashes that resulted from each rotation. Intermolecular clashes (between the protomers of the gating ring) that were introduced by the rotations were assessed with the program NCONT [from the CCP4 Suite (41)]. The count of atom clashes (separation of less than 2.2 Å) was taken as an index of overlap.

ACKNOWLEDGMENTS. We thank Diana Wesch for performing preliminary experiments at early stages of the project, which were not included in this manuscript; Diego Alvarez de la Rosa, Barbara Ehrlich, and Patricio Rojas for helpful comments on the manuscript; Deepa Srikumar for technical assistance; and Jie Zheng for providing the CFP24YFP tandem plasmid. This work was funded by Instituto de Salud Carlos III–Subdirectorate General for Evaluation and Promotion of Research Grants MS07/00034, PI09/00406, and PI12/00428, and Spanish Ministry of Economy Grant Consolider-Ingenio CSD 2008-0005; and cofinanced by the European Regional Development Funds, "A Way of Making Europe," from the European Union (to T.G). Additional support was from the intramural section of the National Institutes of Health (NIH)–National Institute of Neurological Disorders and Stroke (M.H.), Deutsche Forschungsgemeinschaft Grant EXC257 (to A.J.R.P.), and NIH Grant NS21501 (to F.J.S.).

1. Latorre R, Brauchi S (2006) Large conductance Ca^{2+}-activated K^+ (BK) channel: Activation by Ca^{2+} and voltage. *Biol Res* 39(3):385–401.
2. Toro L, Wallner M, Meera P, Tanaka Y (1998) Maxi-K(Ca), a unique member of the voltage-gated K channel superfamily. *News Physiol Sci* 13:112–117.
3. Grimm PR, Irsik DL, Settles DC, Holtzclaw JD, Sansom SC (2009) Hypertension of Kcnmb1−/− is linked to deficient K secretion and aldosteronism. *Proc Natl Acad Sci USA* 106(28):11800–11805.
4. Bloch M, et al. (2007) KCNMA1 gene amplification promotes tumor cell proliferation in human prostate cancer. *Oncogene* 26(17):2525–2534.
5. Yang J, et al. (2010) An epilepsy/dyskinesia-associated mutation enhances BK channel activation by potentiating Ca^{2+} sensing. *Neuron* 66(6):871–883.
6. Díaz L, et al. (1998) Role of the S4 segment in a voltage-dependent calcium-sensitive potassium (hSlo) channel. *J Biol Chem* 273(49):32430–32436.
7. Jiang Y, et al. (2002) Crystal structure and mechanism of a calcium-gated potassium channel. *Nature* 417(6888):515–522.
8. Wang L, Sigworth FJ (2009) Structure of the BK potassium channel in a lipid membrane from electron cryomicroscopy. *Nature* 461(7261):292–295.
9. Yuan P, Leonetti MD, Pico AR, Hsiung Y, MacKinnon R (2010) Structure of the human BK channel Ca^{2+}-activation apparatus at 3.0 A resolution. *Science* 329(5988):182–186.
10. Wu Y, Yang Y, Ye S, Jiang Y (2010) Structure of the gating ring from the human large-conductance Ca^{2+}-gated K^+ channel. *Nature* 466(7304):393–397.
11. Yuan P, Leonetti MD, Hsiung Y, MacKinnon R (2011) Open structure of the Ca^{2+} gating ring in the high-conductance Ca^{2+}-activated K^+ channel. *Nature* 481(7379):94–97.
12. Cox DH, Cui J, Aldrich RW (1997) Allosteric gating of a large conductance Ca-activated K^+ channel. *J Gen Physiol* 110(3):257–281.
13. Rothberg BS, Magleby KL (2000) Voltage and Ca^{2+} activation of single large-conductance Ca^{2+}-activated K^+ channels described by a two-tiered allosteric gating mechanism. *J Gen Physiol* 116(1):75–99.
14. Cui J, Aldrich RW (2000) Allosteric linkage between voltage and Ca^{2+}-dependent activation of BK-type mslo1 K^+ channels. *Biochemistry* 39(50):15612–15619.
15. Horrigan FT, Aldrich RW (2002) Coupling between voltage sensor activation, Ca^{2+} binding and channel opening in large conductance (BK) potassium channels. *J Gen Physiol* 120(3):267–305.
16. Sweet T-B, Cox DH (2008) Measurements of the BKCa channel's high-affinity Ca^{2+} binding constants: Effects of membrane voltage. *J Gen Physiol* 132(5):491–505.
17. Javaherian AD, et al. (2011) Metal-driven operation of the human large-conductance voltage- and Ca^{2+}-dependent potassium channel (BK) gating ring apparatus. *J Biol Chem* 286(23):20701–20709.
18. Lingle CJ (2007) Gating rings formed by RCK domains: Keys to gate opening. *J Gen Physiol* 129(2):101–107.
19. Cui J, Yang H, Lee US (2009) Molecular mechanisms of BK channel activation. *Cell Mol Life Sci* 66(5):852–875.
20. Zheng J, Zagotta WN (2003) Patch-clamp fluorometry recording of conformational rearrangements of ion channels. *Sci STKE* 2003(176):PL7.
21. Giraldez T, Hughes TE, Sigworth FJ (2005) Generation of functional fluorescent BK channels by random insertion of GFP variants. *J Gen Physiol* 126(5):429–438.
22. Heim R (1999) Green fluorescent protein forms for energy transfer. *Methods Enzymol* 302:408–423.
23. Bao L, Rapin AM, Holmstrand EC, Cox DH (2002) Elimination of the BK(Ca) channel's high-affinity Ca^{2+} sensitivity. *J Gen Physiol* 120(2):173–189.
24. Bao L, Kaldany C, Holmstrand EC, Cox DH (2004) Mapping the BKCa channel's "Ca^{2+} bowl": Side-chains essential for Ca^{2+} sensing. *J Gen Physiol* 123(5):475–489.
25. Wei A, Solaro C, Lingle C, Salkoff L (1994) Calcium sensitivity of BK-type KCa channels determined by a separable domain. *Neuron* 13(3):671–681.
26. Schreiber M, Salkoff L (1997) A novel calcium-sensing domain in the BK channel. *Biophys J* 73(3):1355–1363.
27. Schreiber M, Yuan A, Salkoff L (1999) Transplantable sites confer calcium sensitivity to BK channels. *Nat Neurosci* 2(5):416–421.
28. Xia X-M, Zeng X, Lingle CJ (2002) Multiple regulatory sites in large-conductance calcium-activated potassium channels. *Nature* 418(6900):880–884.
29. Zhang G, et al. (2010) Ion sensing in the RCK1 domain of BK channels. *Proc Natl Acad Sci USA* 107(43):18700–18705.
30. Bian S, Favre I, Moczydlowski E (2001) Ca^{2+}-binding activity of a COOH-terminal fragment of the *Drosophila* BK channel involved in Ca^{2+}-dependent activation. *Proc Natl Acad Sci USA* 98(8):4776–4781.
31. Dale RE, Eisinger J, Blumberg WE (1979) The orientational freedom of molecular probes. The orientation factor in intramolecular energy transfer. *Biophys J* 26(2):161–193.
32. Cha A, Bezanilla F (1998) Structural implications of fluorescence quenching in the Shaker K^+ channel. *J Gen Physiol* 112(4):391–408.
33. Hink MA, et al. (2000) Structural dynamics of green fluorescent protein alone and fused with a single chain Fv protein. *J Biol Chem* 275(23):17556–17560.
34. Zheng J, Varnum MD, Zagotta WN (2003) Disruption of an intersubunit interaction underlies Ca^{2+}-calmodulin modulation of cyclic nucleotide-gated channels. *J Neurosci* 23(22):8167–8175.
35. Hu L, Yang H, Shi J, Cui J (2006) Effects of multiple metal binding sites on calcium and magnesium-dependent activation of BK channels. *J Gen Physiol* 127(1):35–49.
36. Qian X, Niu X, Magleby KL (2006) Intra- and intersubunit cooperativity in activation of BK channels by Ca^{2+}. *J Gen Physiol* 128(4):389–404.
37. Villalba-Galea CA, Sandtner W, Starace DM, Bezanilla F (2008) S4-based voltage sensors have three major conformations. *Proc Natl Acad Sci USA* 105(46):17600–17607.
38. Stefani E, et al. (1997) Voltage-controlled gating in a large conductance Ca^{2+}-sensitive K^+ channel (hslo). *Proc Natl Acad Sci USA* 94(10):5427–5431.
39. Bers DM, Patton CW, Nuccitelli R (1994) A practical guide to the preparation of Ca^{2+} buffers. *Methods Cell Biol* 40:3–29.
40. Taraska JW, Zagotta WN (2007) Structural dynamics in the gating ring of cyclic nucleotide-gated ion channels. *Nat Struct Mol Biol* 14(9):854–860.
41. Winn MD, et al. (2011) Overview of the CCP4 suite and current developments. *Acta Crystallogr D Biol Crystallogr* 67(Pt 4):235–242.

Supporting Information

Miranda et al. 10.1073/pnas.1219611110

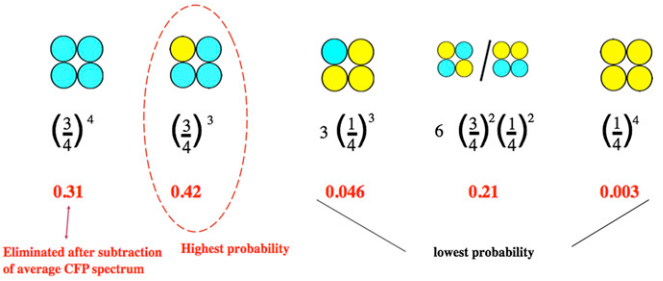

Fig. S1. Subunit combinations forming the heterotetramers. Quantified RNA was injected with CFP-tagged and YFP-tagged BK in a 3:1 ratio. Assuming both RNA types are processed with the same efficiency by the oocyte, it is expected that the probability of tetramer composition follows a binomial distribution given by the expression $p_i = P_Y^i P_C^{n-i}\binom{i}{n}$, where p_i is the probability of i YFP subunits, $n = 4$, and P_Y and P_C are the probabilities of encountering a CFP- or YFP-tagged subunit in the total protein pool, here assumed to be 1/4 and 3/4, respectively. Probabilities of different tetramers are shown below for each possible combination. Highest probabilities are for the 3CFP:1YFP heterotetramer and for the 4CFP homotetramer. Fluorescence from the latter does not contribute to the FRET signal measured.

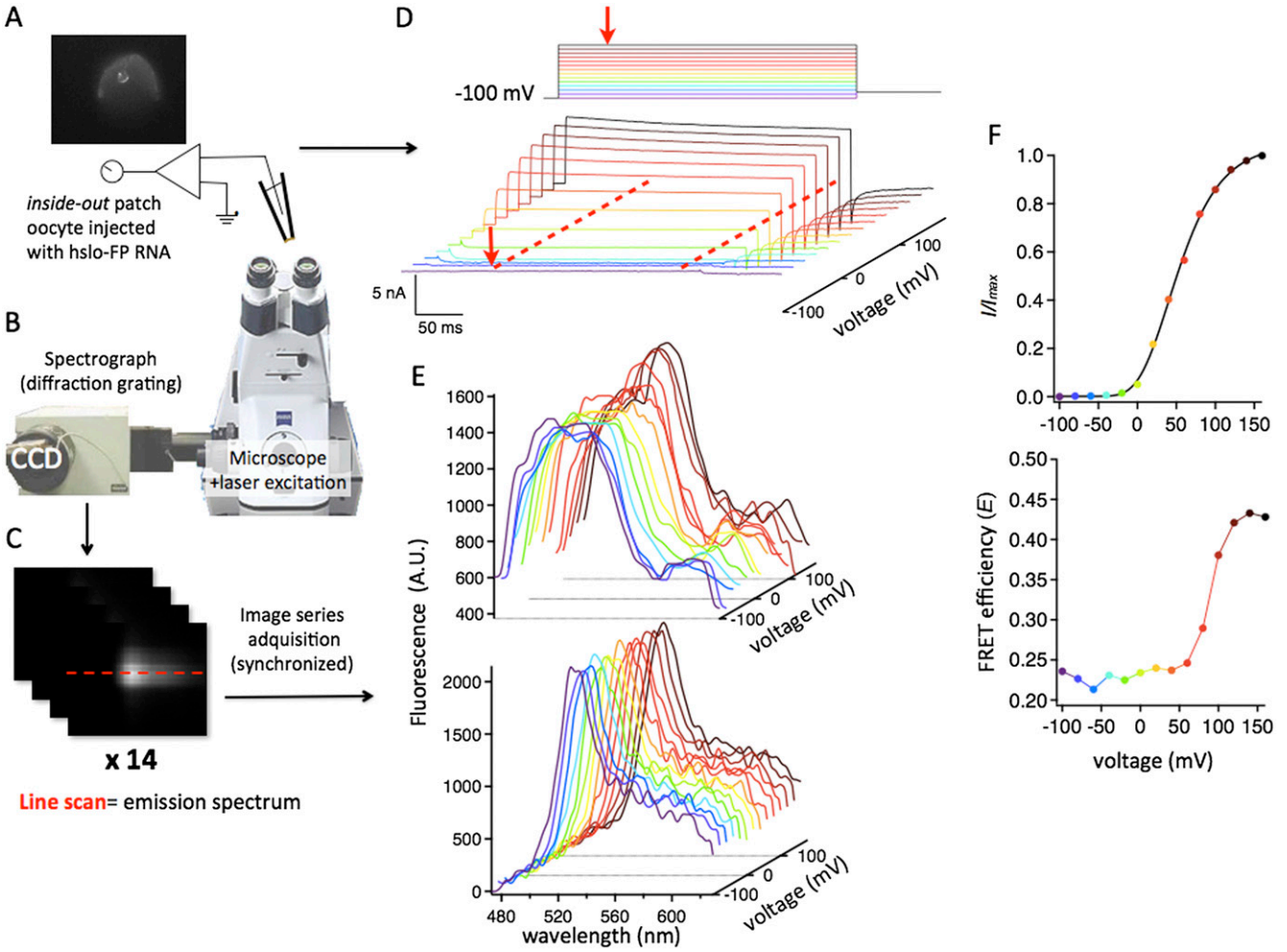

Fig. S2. Spectral-FRET recording from BK channels in membrane patches. (*A*) Inside-out patches are excised from *Xenopus* oocytes microinjected with cRNA combinations of fluorescent large-conductance voltage- and calcium- dependent (BK) channel constructs. Light from the patch is diffracted through the spectrograph (*B*) onto the CCD camera, to obtain spectral images of the patch (*C*). Synchronous optical and electrical recordings show a series of currents (*D*) and spectra (*E*) color-coded according to the voltage steps (−100 to +160 mV). Representative recordings from the construct BK-667YC in 12 μM Ca^{2+} are shown. Spectra (*Upper*, 458-nm excitation, CFP+FRET-YFP; *Lower*, 488-nm excitation, YFP alone) were recorded during steady-state current pulses (red arrow and dashed lines). (*F*) Normalized tail current (*Upper*; proportional to open probability) and FRET efficiency (*E*; *Methods* and Fig. S3) show remarkably similar voltage dependence.

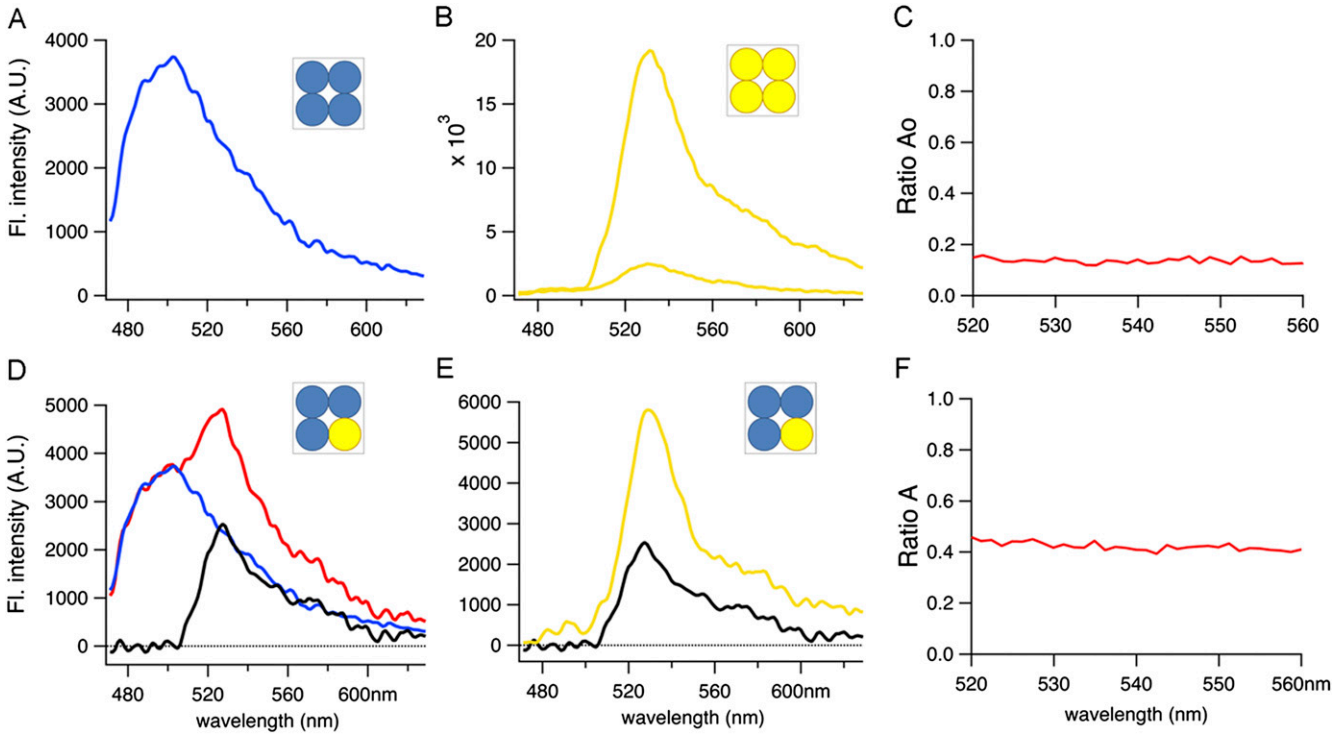

Fig. S3. Spectral analysis procedure. (*A*) Normalized CFP spectrum is obtained as an average from 10 patches expressing BK-CFP. (*B*) Two emission spectra of patches expressing BK-YFP constructs are obtained after excitation at 458 and 488 nm, which are the excitation wavelengths for CFP and YFP, respectively. The 458-nm light does provide some residual excitation of YFP as shown by the lower curve. (*C*) Ratio calculation between spectra in *B* yields the $RatioA_0$ values, which accounts for the direct (no-FRET) YFP excitation. (*D*) The red line represents the spectrum of a patch expressing CFP/YFP combinations. The normalized CFP spectrum (blue line) is first fitted and subtracted. The resulting spectrum (black line) is a combination of direct excitation of YFP at 458 nm plus excitation of YFP by FRET. Finally, this spectrum is compared with the spectrum of the same patch at 488-nm excitation (*E*), which yields RatioA values (*F*). RatioA and $RatioA_0$ are used to calculate the normalized FRET efficiency *E* (*Methods*) (1, 2).

1. Zheng J, Zagotta WN (2003) Patch-clamp fluorometry recording of conformational rearrangements of ion channels. *Sci STKE* 2003(176):PL7.
2. Zheng J, Varnum MD, Zagotta WN (2003) Disruption of an intersubunit interaction underlies Ca^{2+}-calmodulin modulation of cyclic nucleotide-gated channels. *J Neurosci* 23(22): 8167–8175.

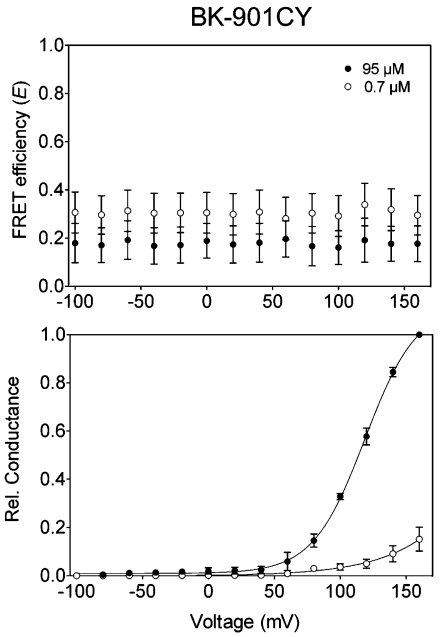

Fig. S4. Patch-clamp fluorometry recording of BK-901 construct. *E–V* (*Upper*) and *G–V* curves (*Lower*) were determined from simultaneous recording of currents and spectra from patches expressing BK-901CY heterotetramers. Data points and error bars represent averages ± SEM ($n = 6$). Ca^{2+} concentrations are indicated in the legend.

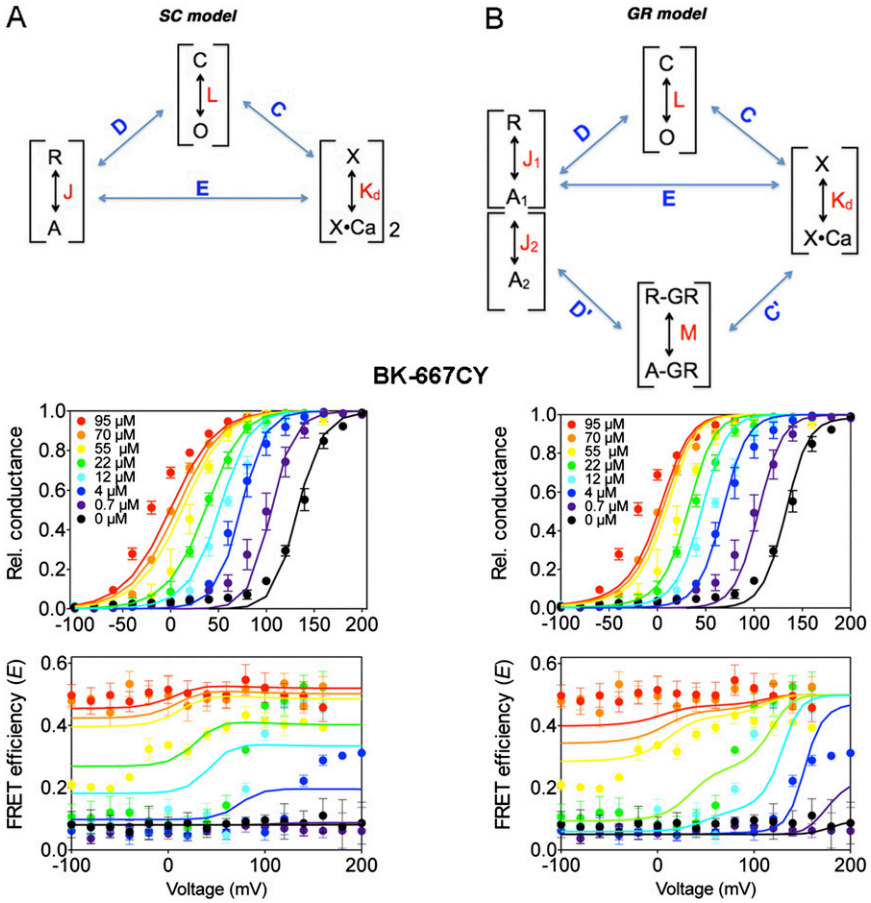

Fig. S5. Simultaneous fitting of gating and FRET signals. (*A*, *Upper*) Sweet and Cox (1) model, which was used to fit the *G–V* curves in Figs. 3*A* and 4*A*. In each subunit, two calcium binding sites are coupled to the resting↔activated transition of a voltage sensor (allosteric constant *E*), and each of these is coupled to the concerted closed↔open transition for the ion channel (allosteric constants *C* and *D*). (*A*, *Lower*) Application of this model (solid curves) to simultaneously describe the *G–V* and *E–V* data obtained in this study. Whereas *G–V* curves are well fitted using this model, it does not correctly predict the *E–V* data. The steady-state parameters that give rise to the solid curves are V_h (*J*) = 148 mV, $z_J = 0.58$ e, $L_0 = 2.2 \times 10^{-6}$, $z_L = 0.42$ e, $K_{d1} = 4.1$ μM, $K_{d2} = 39$ μM, $C_1 = 3.6$, $C_2 = 6.16$, $D = 30.4$, $E_1 = 1$, $E_2 = 2.1$, where *J, K*, and *L* are the equilibrium constants for voltage sensor activation, Ca^{2+} binding, and C-O transition, respectively; V_h (J) is the voltage where $J = 1$; L_0 and z_J are the zero voltage value of *L* and its partial charge, respectively; K_{d1} and K_{d2} are the Ca^{2+} dissociation constants, and C_1, C_2, *D*, E_1, and E_2 are the allosteric constants describing channel opening/Ca^{2+} binding, channel opening/voltage sensor activation, and voltage sensor activation/Ca^{2+} binding interactions, respectively (1, 2). (*B*) An example showing our attempts to modify the allosteric model to fit our results. In this example (*Upper*), we assumed that each of the four voltage sensor domains, once activated, can undergo a "relaxation" step, as has been seen in various S4-type voltage sensors (3), but for which there is no evidence currently for the BK channel. Whereas the first transition (equilibrium constant J_1) is coupled to Ca^{2+} binding and channel opening (allosteric constants *D* and *E*), the second transition (equilibrium constant J_2) is coupled to a concerted conformational change of the gating ring (GR) that has a basic equilibrium constant *M*. It is the probability p_A of this activated state that affects FRET efficiency. For every voltage sensor in state A_2 and every binding site with Ca^{2+} bound, the GR equilibrium is increased by the factors *D′* and *C′*, respectively. Although this model gave the best description of those we tried, it predicts complicated gating currents and more work is required to investigate how well these predictions correspond to the actual biophysical properties of the BK channel. (*B*, *Lower*) Description of the Ca^{2+} and voltage dependence of both the channel opening and the FRET signal (solid lines) provided with the scheme *B* expanded to include two Ca^{2+} binding sites in each subunit. The parameter values that give rise to the curves in *B* are as follows: $V_h(J_1)$ = 148 mV, $V_h(J_2)$ = 160 mV, $z_{J1} = 0.58$ e, $z_{J2} = 1.5$ e, $K_{d1} = 4$ μM, $K_{d2} = 100$ μM, $L_0 = 5.41 \times 10^{-6}$, $z_L = 0.41$ e, $C_1 = 6.12$, $C_2 = 1.92$, $D = 25$, $E_1 = 1$, $E_2 = 1.2$, $C_1' = 1.33$, $C_2' = 20.2$, $D' = 6$, and $M = 0.0001$. Modeling methods: Calculation of the open probability and the energy transfer efficiency for a wide range of models was done with a MATLAB program that could include multiple concerted transitions, binding sites, and voltage sensors. In a brute-force approach, we used matrix algebra to compute the partition function and thereby the probability of each state for a given Ca^{2+} concentration and membrane potential. Through various optimizations, we were able to work with models having more than 2^{20} states. The sum of the probabilities of the states in which the channel is open provided the open probability values, which were compared with *G–V* data. For the models shown here, the underlying FRET changes assumed only two values, *E* was obtained as $E = E_R + p_A(E_A - E_R)$, where E_R is the resting FRET efficiency, E_A is the active-state efficiency, and p_A is the probability of active states at a given voltage and calcium concentration.

1. Sweet T-B, Cox DH (2008) Measurements of the BKCa channel's high-affinity Ca^{2+} binding constants: Effects of membrane voltage. *J Gen Physiol* 132(5):491–505.
2. Horrigan FT, Aldrich RW (2002) Coupling between voltage sensor activation, Ca^{2+} binding and channel opening in large conductance (BK) potassium channels. *J Gen Physiol* 120(3): 267–305.
3. Villalba-Galea CA, Sandtner W, Starace DM, Bezanilla F (2008) S4-based voltage sensors have three major conformations. *Proc Natl Acad Sci USA* 105(46):17600–17607.

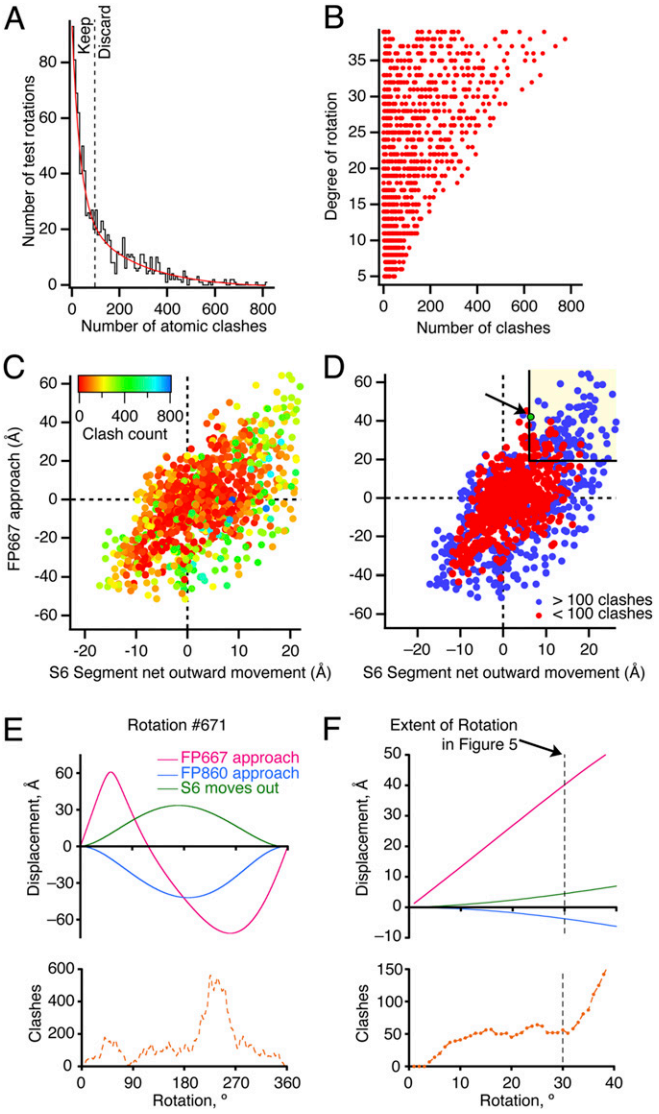

Fig. S6. Statistics of candidate models for gating-ring motion. (*A*) The distribution of 1,000 models formed by random rotations of gating-ring subunits. The histogram shows the number of atomic clashes (proximity, <2.2 Å). Clashes between two immediately adjacent subunits (~10,000 atoms) were assessed. Many models had few clashes, and the cutoff (dashed line) was set at 100 clashes, or about 1% of the total atoms considered. (*B*) The number of clashes for the 1,000 models plotted against the magnitude of rotation, in degrees. All rotation extents gave some models with a small number of clashes, but large, physically nonsensical clash counts only occurred for large rotations. (*C*) For each model is plotted the expected approach of the fluorescent proteins inserted at 667, and the expected movement of the S6 segment. The color of each point represents the count of clashes. (*D*) Simplified version of *C*, showing the models with less than 100 clashes as red dots. Only 26 models sit in the shaded area for which the gate moved >6 Å, and the approach of the fluorescent proteins was >20 Å. Most of these models were implausible as they either (*i*) brought the 860 insertions much closer together, opposite to the FRET signal we observed, or (*ii*) were only reached following substantial clashes during the rotation. Relative position of model shown in Fig. 5 (*Right*) is indicated with a green circle and arrow. (*E*) Clashes, fluorophore positions, and S6 linker of a full 360° rotation of the each subunit around the axis used to generate the model in Fig. 5. Steric clashes between fluorophores were not assessed, and 30° rotation brought the insertions at 667 to their closest possible extent. (*F*) Same plot as *E* but on an expanded scale.

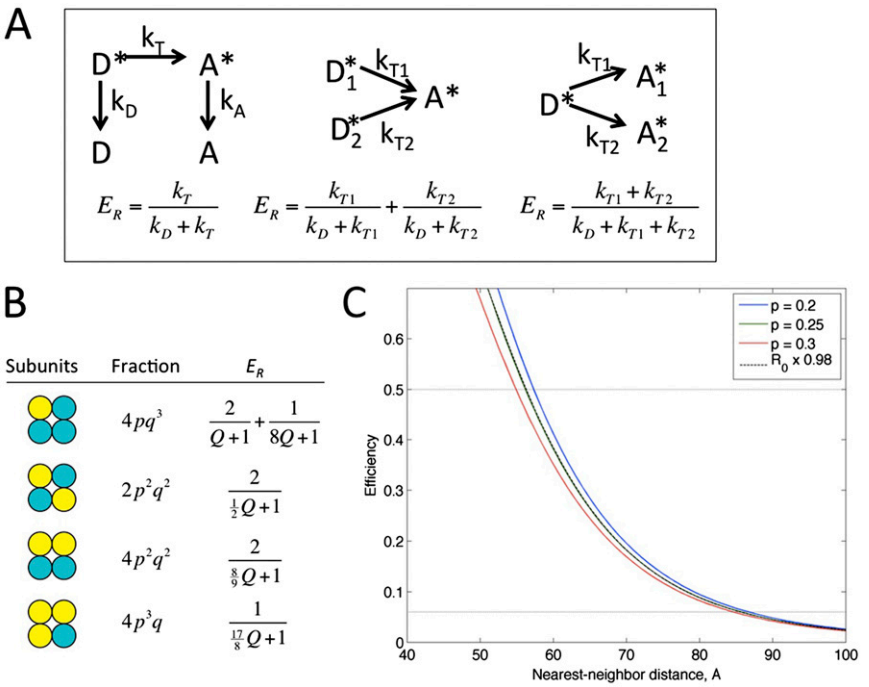

Fig. S7. Energy transfer among equivalent positions in a tetrameric protein with C4 symmetry. (*A*, *Left*) Acceptor emission intensity E_R relative to that of a single donor–acceptor pair at zero separation. E_R depends on the donor decay rate k_D and the transfer rate constant k_T, which are related to the Förster distance R_0 according to $\frac{k_D}{k_T}=\left(\frac{r}{R_0}\right)^6$. (*A*, *Center*) Assuming that the excitation intensity is well below saturation of the fluorophores (as was the case in our experiments), the combination of two donors and one acceptor yields the sum of individual FRET intensities. (*A*, *Right*) The emission from the combination of one donor and two acceptors is described by adding the two transfer rate constants. (*B*) Contributions E_R to the emission intensity from each configuration of subunits. The probability of a YFP subunit in any position is p and the corresponding CFP probability $q=1-p$. The Förster ratio is $Q=k_D/k_T$. (*C*) Energy transfer efficiency as a function of fluorophore spacing, assuming $R_0=50$ Å. The weighted sum of the E_R, normalized by the average number of YFP subunits ($4p$ in this case) gives the FRET efficiency E as defined in the main text. This is plotted as a function of nearest-neighbor distance for three values of p, representing a range of relative expression levels of the CFP and YFP subunits centered on $P=0.25$. The dotted curve (largely hidden by the $P=0.25$ curve) shows the values of E given by the fitted function: $E=\frac{1.4}{\left(\frac{0.98r}{R_0}\right)^6+1}$. The horizontal lines show the values $E=0.06$ and $E=0.5$ observed at extremes of Ca^{2+} concentration with the 667 construct.

Table S1. *G–V* fitting parameters

Parameter	BK860CY (Fig. 3*A*)	BK667CY (Fig. 4*A*)	BK667/5D5A/CY (Fig. 4*B*)	BK667/5D5A/M513I/CY (Fig. 4*C*)
V_h(J), mV	148	148	148	148
z_J, e	0.58	0.58	0.58	0.58
L_0	2.2×10^{-6}	2.2×10^{-6}	2.2×10^{-6}	2.2×10^{-6}
z_L, e	0.42	0.42	0.42	0.42
K_{d1}, μM	4.1	4.1	900	900
K_{d2}, μM	39	39	39	900
C_1	3.34	3.6	1	1
C_2	5.25	6.16	11.03	137.35
D	29.87	30.37	2.86	2.05
E_1	1	1	1	1
E_2	2.29	2.13	26.16	3.07

Column 1 (BK860CY), steady-state parameters used to compute *G–V* curves in Fig. 3*A* (*Upper*), modified from the Sweet and Cox (1) model, which is an extension of the Horrigan and Aldrich (2) model to include two Ca^{2+} binding sites. Columns 2–4 show the parameters used to compute the *G–V* curves in Fig. 4 *A–C* (*Upper*) for the BK667CY constructs indicated in the column titles. *J*, *K*, and *L* are the equilibrium constants for voltage sensor activation, Ca^{2+} binding, and C-O transition, respectively; V_h (*J*) is the voltage, where $J=1$; L_0 and z_J are the zero voltage value of *L* and its partial charge, respectively; K_{d1} and K_{d2} are the Ca^{2+} dissociation constants; and C_1, C_2, *D*, E_1, and E_2 are the allosteric constants describing channel opening/Ca^{2+} binding, channel opening/voltage sensor activation, and voltage sensor activation/Ca^{2+} binding interactions, respectively (1, 2).

1. Sweet T-B, Cox DH (2008) Measurements of the BKCa channel's high-affinity Ca^{2+} binding constants: Effects of membrane voltage. *J Gen Physiol* 132(5):491–505.
2. Horrigan FT, Aldrich RW (2002) Coupling between voltage sensor activation, Ca^{2+} binding and channel opening in large conductance (BK) potassium channels. *J Gen Physiol* 120(3): 267–305.